

# Simulation of Mechanical Compression of Breast Tissue

Albert L. Kellner, Thomas R. Nelson\*, *Member, IEEE*, Laura I. Cerviño, and John M. Boone, *Member, IEEE*

**Abstract**—Comparison of uncompressed volumetric breast data to compressed projection mammographic data poses a variety of challenges to accurately localize anatomy in both data sets. This work presents a method for simulating the mechanical compression of volumetric breast data. We use an approach based on a rectilinear-grid finite-element mesh and apply the method to known objects including volumetric breast data. Overall results show good agreement with theory and reasonable qualitative agreement with clinical results. Analysis times are sufficiently short to be used in the clinical setting for data comparison. The methods presented here provide a high quality method for simulating mechanical compression of breast data.

**Index Terms**—Breast, compression, computed tomography, finite-element analysis.

## I. INTRODUCTION

COMPUTED TOMOGRAPHY (CT) of the breast is potentially a high-sensitivity replacement for conventional projection mammography [1]. Comparing the relative clinical performance of volumetric breast CT and compression mammography images requires simulating mechanical compression of the breast. Cranio-caudal (CC) and medio-lateral oblique (MLO) compression views are most often used clinically for identification and localization of breast tumors. The CC and MLO views can be simulated by applying numerical mechanical compression to the volume data so that features can be located and identified on these views and compared to the standard clinical projection images.

In this paper we present a method of simulating the mechanical compression of the breast, which is ideally suited for use with volumetric CT data. This method consists of the segmentation and classification of the volumetric data into several material types, coupled with a finite-element (FE) algorithm modified from an approach originally developed to compute the effective linear elastic properties of heterogeneous composites with distributed microstructures (such as concrete) [2]–[4]. An advantage of this method is that the mesh is a simple cubic lattice where each finite element is piece-wise

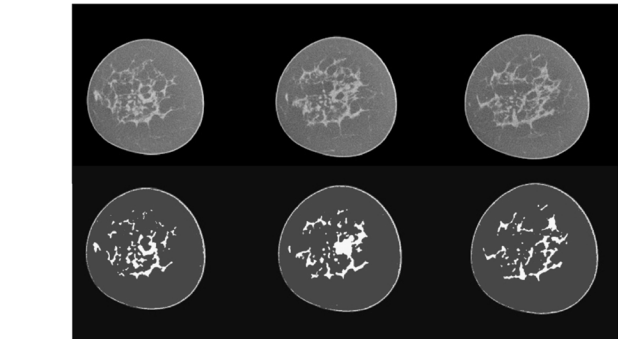


Fig. 1. Selected original and segmented images from breast CT scan data for a typical breast. (a) Upper panel: mid-breast image slices. (b) Lower panel: same three slices as upper panel after classification.

constant corresponding to voxel data, making this method well suited to the volumetric data obtained from breast CT.

After a discussion of the methodology, we present data from several numerical simulations, including breast CT data, to assess the performance of the algorithm. We also present simulations of CC view projection mammograms.

## II. BREAST COMPRESSION CONSIDERATIONS

Among the primary challenges in simulating mechanical compression of the breast are classification of the various tissues in the breast, description of the mechanical properties of the tissues in the breast, and selection of the appropriate numerical algorithm for compression.

### A. Breast Tissue Data Acquisition

We have developed a dedicated breast CT scanner that produces high-resolution volumetric images of pendant breasts [1]. The scanner produces a series of approximately 300  $512^2$  image slices with a nominal resolution of  $250\ \mu\text{m}$ . The resulting images are embedded into a  $512^3$  cubic volume. After receiving Investigational Review Board approval and informed consent, we imaged a limited series of normal volunteers and patients with mammographically confirmed breast cancer at UC Davis. The images produced by this scanner subjectively are of higher quality than projection mammography [5]. The average glandular dose per breast is approximately the same as that for conventional two-view mammography [5]. Typical uncompressed original data are shown in Fig. 1(a).

### B. Breast Tissue Classification

The normal breast consists of a tree-like structure of glandular tissue supported by a network of connective tissues cushioned by fat and surrounded by skin. With age, especially after

Manuscript received February 3, 2006; revised January 24, 2007. This work was supported in part by California Breast Cancer Research Program Grant 7EB-0075, NIH Grants 11IB-0035, NCI-R01 CA89260, and NIBIB-EB002138, and the Susan G. Komen Foundation. Asterisk indicates corresponding author.

A. L. Kellner is with the Department of Electrical and Computer Engineering, University of California at San Diego, La Jolla, CA 92093-0407 USA.

\*T. R. Nelson is with the Department of Radiology, University of California at San Diego, La Jolla, CA 92037-0610 USA (e-mail: tnelson@ucsd.edu).

L. I. Cerviño is with the Department of Radiology, University of California at San Diego, La Jolla, CA 92037-0610 USA.

J. M. Boone is with the Department of Radiology, University of California at Davis, Sacramento, CA 95817 USA.

Digital Object Identifier 10.1109/TBME.2007.893493

menopause, the distribution of breast tissues changes from predominately glandular tissues to predominately fatty tissues. The radiographic characteristics of breast tissue are such that tumors exhibit similar properties to glandular tissue.

Analysis of breast tissue raises the question of defining how many components, or phases, are sufficient to describe the tissue in question. It is common to treat the breast as partially homogeneous wherein the fat and glandular tissue have one set of mechanical properties and the skin has a second set [6]. For this work, we use a model of the breast consisting of three materials: skin, fat, and glandular tissue.

The tissue types are classified following the method of Nelson *et al.* [7]. In summary, image slices are filtered using a five-point median filter and the image histogram is computed. Since skin and glandular tissue have similar CT values we use a two-compartment Gaussian fit of the histogram data. The Gaussian fit provides an initial estimate of the different tissue compartments in the slice based on the thresholded voxel value. After the histogram classifier, a seed point is identified for input to a region-growing algorithm. Voxels are classified as belonging to skin, fat, or gland based on their voxel values and architectural features [Fig. 1(b)].

### C. Tissue Elastic Model

Once the components have been identified, it becomes important to consider the particular elastic model used for each component. A challenge is to determine the mechanical model and coefficients to use that represent the physical properties of the tissues with sufficient accuracy that the analysis results are useful. The complexity of biological tissues necessitates trade-offs between higher accuracy and longer computational times in the selection of the appropriate algorithm.

There are four models most often used to represent the elastic properties of breast tissues: linear (Hookean), Mooney–Rivlin, exponential, and power series. Ruiter [8] presents an excellent review and analysis of various mechanical models of breast tissue. In summary, she notes that the accuracy of a finite-element based simulation is not significantly affected when using simpler material models and low strains.

A linear model was used by Bakic *et al.* [9] to demonstrate the synthesis of projection mammograms from MR data sets, and by Schnabel *et al.* [10] to demonstrate the nonrigid registration of breast MR volumes under mechanical compression and the simulation of mechanical compression. Although few biological materials obey Hooke's law [11, p. 38], a linear model often provides a sufficiently accurate approximation. Tanner *et al.* [6] conclude that displacement errors are not highly dependent on the material models chosen for the tissues of the breast, with a linear approximation being an adequate choice. In this work we will use the linear model.

### D. Material Coefficients

As noted above, we used a three-compartment breast model (skin, fat, and gland) where each component is treated as a linear (Hookean) material with material coefficients obtained from Schnabel *et al.* [10], Sarvazyan *et al.* [12], Park [13], and Tanner *et al.* [6]. These coefficients are given in Table I.

TABLE I  
ELASTIC PROPERTIES OF BREAST TISSUE USED FOR SIMULATIONS.  
COEFFICIENTS OBTAINED FROM SCHNABEL *et al.* [10], SARVAZYAN *et al.* [12],  
PARK [13], AND TANNER *et al.* [6]

Material	Young's modulus	Poisson's ratio
Skin	88.0 kPa	0.490
Fat	1.0 kPa	0.490
Glandular	10.0 kPa	0.490

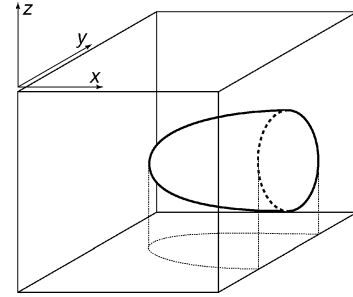


Fig. 2. Geometry of the breast compression problem. Breast is embedded in a cubic volume.

Material properties for Table I were obtained from *in vitro* and *in vivo* elastic coefficient measurements. *In vitro* measurements can vary significantly depending on preparation, hydration, etc. Also, there can be substantial variability in tissue properties between individuals affecting *in vivo* measurements. As a result, variations between individuals are potentially larger than the error in a particular material model.

### E. Compression Model Mesh Geometry

Finite-element models of the breast typically either use two-dimensional elements defined on the surface of the breast [14]–[16] or three-dimensional elements defined in the volume of the breast. Three-dimensional elements can be defined by nodes described by the *structure* [6], or by nodes described by the *volume* [2]–[4]. The challenge is defining the organization of the finite-element mesh to best capture the structure of the breast while minimizing the complexity of the computation.

We used a multidimensional rectilinear mesh defined over the entire volume. The finite elements correspond to the voxels in the volume [2]–[4]. For this method, the structure was segmented into its constituent parts as described above, but the segments were not required to be contiguous. Each node in the mesh relates to a material property based on this segmentation.

Since the rectilinear mesh matches the organization of volumetric breast CT data, this significantly reduces the difficulty in describing the geometry of the individual breasts analyzed.

## III. MECHANICAL COMPRESSION ALGORITHM

### A. Algorithm

Consider that the breast tissue is embedded in a cubic volume  $\mathbb{R}^3$  of air, where the chest wall corresponds to the right-most  $y$ - $z$  plane and cranio-caudal (CC) compression corresponds to compression along the  $z$  direction (Fig. 2).

Let the breast tissue be composed of  $n$  independent phases, or types, of isotropic, linear elastic material, for instance skin,

fat, and gland. The mechanical properties of each phase are governed by Hooke's law:

$$\sigma_{ij} = \sum_{k \in (x,y,z)} \left[ \lambda^{(m)} \varepsilon_{kk} \delta_{ij} \right] + 2\mu^{(m)} \varepsilon_{ij}, \quad \text{for } i, j = (x, y, z) \quad (1)$$

where  $\sigma_{ij}$  is the locally applied stress,  $\varepsilon_{ij}$  is the local strain,  $\delta_{ij}$  is the Kronecker delta, and  $\lambda^{(m)}$ ,  $\mu^{(m)}$  are the Lamé constants of the  $m$ th material phase, given by [17, pp. 157–161]:

$$\lambda^{(m)} = \frac{Y^{(m)} \nu^{(m)}}{(1 + \nu^{(m)}) (1 - 2\nu^{(m)})} \quad (2)$$

$$\mu^{(m)} = \frac{Y^{(m)}}{2(1 + \nu^{(m)})} \quad (3)$$

$Y^{(m)}$  and  $\nu^{(m)}$  are the Young's modulus and Poisson's ratio, respectively, of the  $m$ th phase. The second Lamé constants,  $\mu^{(m)}$ , are identical to the shear modulus  $G^{(m)}$  of each material phase.

Eq. (1) can be rewritten in terms of the elasticity tensor  $\mathbf{C}^{(m)}$  of the  $m$ th material phase

$$\underline{\underline{\sigma}}^{(m)} = \mathbf{C}^{(m)} \cdot \underline{\underline{\varepsilon}}^{(m)} \quad (4)$$

where  $\underline{\underline{\sigma}}^{(m)}$  is the local microscopic stress tensor and  $\underline{\underline{\varepsilon}}^{(m)}$  is the local microscopic strain tensor of the  $m$ th material phase.

The elasticity tensor  $\mathbf{C}^{(m)}$  can be written in terms of the Lamé coefficients using Voigt notation:<sup>1</sup>

$$\mathbf{C} = \begin{pmatrix} \lambda + 2\mu & \lambda & \lambda & 0 & 0 & 0 \\ \lambda & \lambda + 2\mu & \lambda & 0 & 0 & 0 \\ \lambda & \lambda & \lambda + 2\mu & 0 & 0 & 0 \\ 0 & 0 & 0 & 2\mu & 0 & 0 \\ 0 & 0 & 0 & 0 & 2\mu & 0 \\ 0 & 0 & 0 & 0 & 0 & 2\mu \end{pmatrix} \quad (5)$$

Equivalently, the stress tensor  $\underline{\underline{\sigma}}^{(m)}$  and the strain tensor  $\underline{\underline{\varepsilon}}^{(m)}$  also can be written using Voigt notation:

$$\underline{\underline{\sigma}}^{(m)} = \begin{pmatrix} \sigma_{xx} \\ \sigma_{yy} \\ \sigma_{zz} \\ \sigma_{xy} \\ \sigma_{yz} \\ \sigma_{zx} \end{pmatrix} \quad \underline{\underline{\varepsilon}}^{(m)} = \begin{pmatrix} \varepsilon_{xx} \\ \varepsilon_{yy} \\ \varepsilon_{zz} \\ \varepsilon_{xy} \\ \varepsilon_{yz} \\ \varepsilon_{zx} \end{pmatrix}. \quad (6)$$

The stored strain energy  $W$  of the tissue in Fig. 2 is

$$W = \frac{1}{2} \int_{\mathbb{R}^3} \underline{\underline{\varepsilon}}^{(m)} \cdot \mathbf{C} \cdot \underline{\underline{\varepsilon}}^{(m)} d^3 r \quad (7)$$

or using Voigt notation

$$W = \frac{1}{2} \int_{\mathbb{R}^3} \sum_{i,j} \varepsilon_i(\underline{r}) C_{ij}^{(m(\underline{r}))} \varepsilon_j(\underline{r}) d^3 \underline{r} \quad (8)$$

where  $\underline{r} = (x, y, z)$ .

<sup>1</sup>In the Voigt notation, the indices (1, 2, 3, 4, 5, 6) correspond to the indices (xx, yy, zz, xy, yz, zx), respectively, so, for example,  $C_{11} = C_{xx,xx}$ .

The data output from the breast CT scanner is a cubic array of voxels. Using piecewise constant finite elements defined on a rectilinear mesh covering  $\mathbb{R}^3$ , (8) can be reduced to

$$W = \frac{1}{2} \sum_{n=1}^N \sum_{i,j=1}^6 \varepsilon_{i,n} C_{ij}^{(n)} \varepsilon_{j,n} \quad (9)$$

where  $N$  is the number of voxels in  $\mathbb{R}^3$ .

Eq. (9) can be rewritten from using local strains  $\varepsilon_{i,j}$  to using local displacements  $u_{i,j}$  [3, pp. 12–14]:

$$W = \frac{1}{2} \sum_{rp,sq} u_{rp}^T D_{rp,sq} u_{sq} \quad (10)$$

where  $u_{sq}$  is the  $q$ th component of the displacement  $\underline{u}_s$  of the  $s$ th node, and  $D_{rp,sq}$  are the components of the stiffness matrix, given by

$$D_{rp,sq} = \int_{\mathbb{R}^3} S_{\alpha,rp}^T C_{\alpha\beta} S_{\beta,sq} d^3 r \quad (11)$$

where  $S_{\beta,sq}$  relates the effects of local strain between each pair of finite elements.

## B. Boundary Conditions

The voxels in the plane corresponding to the chest wall (the right-most  $y$ - $z$  plane) are constrained so their  $x$  coordinates are fixed.

Compression is applied to the top-most and bottom-most  $x$ - $y$  planes by setting boundary conditions on these planes. The voxels in the top-most  $x$ - $y$  plane initially are set so their  $z$ -coordinates correspond to the applied macroscopic strain  $\varepsilon_{\text{macro}}$ ; the voxels on the bottom-most  $x$ - $y$  plane initially are set so their  $z$ -coordinates are zero. The compressive forces are transferred to breast tissue by embedding the breast in “air”; that is, by setting the material properties of the nonbreast voxels to highly-compressible material (low Young's modulus) with a Poisson's ratio of zero.

The voxels on the remaining three boundary planes are unconstrained.

## C. Algorithm Convergence Criteria

A conjugate gradient technique [18, pp. 301–306] is used to find the minimum strain energy  $W$  given by (10), with respect to variations in the nodal displacements  $\underline{u}_s$ .

There are several methods of determining when a local solution minimum is obtained:

- 1) when the change in strain energy  $W$ , from iteration to iteration, is less than some tolerance  $\epsilon$

$$\Delta W < \epsilon; \quad (12)$$

- 2) when the magnitude of the gradient of the strain energy with respect to the nodal displacements is less than some tolerance  $\epsilon$

$$|\nabla W| < \epsilon; \quad (13)$$

- 3) when the mean change in the square of the displacement of each node  $u_i$  in the structure of interest, from iteration to iteration, is less than some tolerance  $\epsilon$

$$\frac{1}{M} \sum_i |\Delta \underline{u}_i|^2 < \epsilon \quad \forall u_i \in \{\text{structure}\} \quad (14)$$

where  $M$  is the number of nodes (voxels) in the structure of interest, and  $\Delta \underline{u}_i$  is the change in  $\underline{u}_i$  between two sequential iterations. The “structure of interest” is, as an example, the breast tissue (fat, skin, and gland) or the glandular tissue only.

The second method using the gradient magnitude, is traditionally used. However, the scaling of the strain energy function is highly sensitive to the matrix size and input parameters, such as Young’s moduli, Poisson’s ratios, and material distribution. This makes it difficult *a priori* to set a convergence tolerance.

The third method based on using nodal displacements is more robust, also permitting a convergence tolerance to be set *a priori*. This also matches our goal of defining convergence when voxels no longer move between iterations. However, based on our observations from numerous simulations over several data sets, we find that a minimum number of iterations, approximately equal to twice the linear mesh dimension, is required for stability at small applied compressive strains  $\epsilon_{\text{macro}}$ . We used this method for assessing the convergence.

#### D. Algorithm Implementation

To implement the algorithm discussed in Section III-A, we follow this sequence.

- 1) Three-dimensional voxel data are obtained from patients scanned in a dedicated breast CT scanner in the pendant orientation.
- 2) 512 image slices, each with a resolution of  $512^2$  pixels, are segmented into skin, fat, and glandular tissue [7]. The embedding media (the nonbreast voxels) is considered “air”, with a corresponding Young’s modulus.
- 3) The image slices are stacked together and down-sampled, forming a volume of  $128^3$  voxels. The down-sampling is performed by selecting the tissue type corresponding to the coordinates of the down-sampled voxel.
- 4) Segmented material properties are assigned using the values given in Table I.
- 5) A homogeneous macroscopic strain  $\epsilon_{\text{macro}}$  is applied along the appropriate direction (e.g., the  $z$ -axis for CC projection).
- 6) Using a strain-energy function as given by (10) and (11), the conjugate gradient algorithm is iterated for a minimum number of steps, or until convergence as given by (14) is reached.
- 7) Macroscopic stress  $\sigma_{\text{macro}}$ , local microscopic stresses, strains, and nodal displacements  $\underline{u}_i$  are calculated.

The local stresses are obtained by multiplying the local strain tensor of each voxel (calculated by the conjugate gradient algorithm) by the local elasticity matrix of each voxel (calculated from the local Young’s modulus and Poisson’s ratio). The macroscopic stress  $\sigma_{\text{macro}}$  is calculated from the vector sum of the local stresses.

- 8) An effective Young’s modulus of the structure  $Y_{\text{eff}}$  is determined from the applied macroscopic strain  $\epsilon_{\text{macro}}$  and the calculated macroscopic stress  $\sigma_{\text{macro}}$ , where

$$Y_{\text{eff}} = \frac{\sigma_{\text{macro}}}{\epsilon_{\text{macro}}} \quad (15)$$

- 9) The voxel spatial coordinates of the mechanically compressed volumes are calculated from the nodal displacements  $\underline{u}_i$  and upsampled from  $128^3$  to  $512^3$  for comparison to the original CT data.
- 10) For display of the mechanically compressed *segmented* volumes, we either used the segmented values by assigning a grey-level to each tissue type (skin, fat, or glandular) or we assigned the grey-level from the corresponding voxel of the original unsegmented volume.

#### IV. SIMULATION RESULTS

We evaluated a variety of simple objects plus a segmented breast to validate the method and refine the analytical methodology.

##### A. Algorithm Simulation Results

In this section we review simulation results for a rectangular beam, a spherical shell, and breast data. The FE mesh was comprised of  $128^3$  (2 097 152) elements. Simulations were performed with incremental initial strains ranging from 0.0 to 0.7. A convergence tolerance of  $10^{-7}$  was used per (14). Using a dual 2.7 GHz PowerPC G5 with 4 GByte RAM (Apple, Cupertino, CA) using a single processor, computation times ranged from 1 to 40 min scaling with the applied strain and geometrical complexity. Simulations were compared to theory when appropriate, and qualitatively to clinical results.

1) *Rectangular Beam*: A rectangular beam, with a  $z$ -axis height of 128 (voxel) units, and a width and breadth of 64 units was embedded in a  $128^3$  voxel space. The beam and surrounding material had a Young’s modulus of 2.0 kPa and a Poisson’s ratio of 0.490 [Fig. 3(a)].

The volume stress-strain relationship [Fig. 3(b)] and the transverse ( $x$ - and  $y$ -axes) widths obtained from the simulation (Fig. 4) were compared to theory showing excellent agreement ( $\rho = 0.999$ ).

2) *Spherical Shell*: A spherical shell with an outer diameter of 84 units and a skin thickness of 2.5 units was embedded in a  $128^3$  space. In the first set of simulations the shell and the surrounding material had a Young’s modulus of 2.0 kPa and a Poisson’s ratio of 0.490.

Cross-section views of the changes in geometry and the stress-strain relationships are displayed in Fig. 5. There is excellent agreement ( $\rho = 0.999$ ) between the value of Young’s modulus calculated by the algorithm simulation (2.00 kPa) and theory (2.00 kPa).

Next we changed the value of the Young’s modulus of the shell to 90.0 kPa, comparable to skin, leaving the Young’s moduli of the exterior and interior regions at 2.0 kPa. Cross-section views of the changes in geometry and the stress-strain relationships are displayed in Fig. 6.

The sphere becomes more flattened with compression than in the case where the Young’s modulus of the spherical shell is

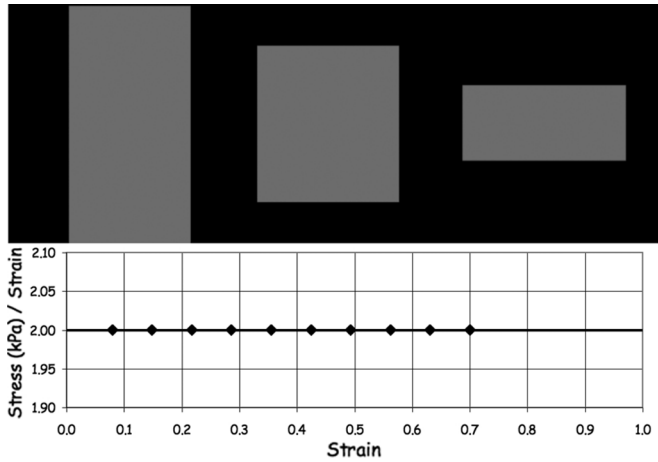


Fig. 3. Comparison of simulation with theory for rectangular beam. The beam and surrounding material had a Young's modulus of 2.0 kPa and a Poisson's ratio of 0.490. (a) Upper panel: a subset of the 10 steps showing the response to variations in the initial applied strain  $\varepsilon_{\text{macro}}$  at values of 0.0, 0.35 and 0.70. (b) Lower panel: comparison of simulation (symbol) with theory (line) showing excellent agreement (correlation coefficient ( $\rho$ ) = 1.00).

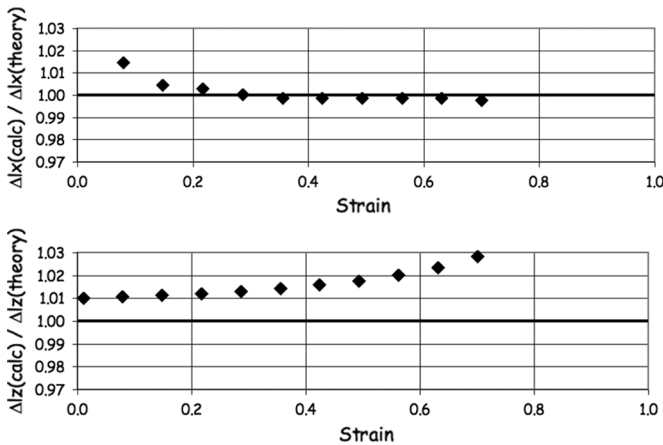


Fig. 4. Comparison of simulation with theory for simple rectangular beam. The plots depict the ratio of the fractional change in  $\Delta\ell_x$ ,  $\Delta\ell_y$  and  $\Delta\ell_z$  for the simulation divided by the theoretical values for the physical parameters and geometry used in the simulation. (a) Upper panel:  $\Delta\ell_x(\text{calculation}) / \Delta\ell_x(\text{theory})$ . The results for the  $y$  direction were the same. (b) Lower panel:  $\Delta\ell_z$  direction. The solid line denotes agreement between simulation and theory. The deviation from theory is related to truncation errors associated with the finite dimensions of the simulation. This effect is most noticeable in the  $x$  and  $y$  directions when relatively little strain is applied as the displacements are small fractions of a voxel dimension. The opposite is noted in the  $z$  direction where the truncation in the smaller compressed matrix are more apparent. In both cases the deviations are within 3%.

comparable to that of the interior and exterior regions. This suggests the importance of the larger elastic moduli of the skin compared to fat and glandular tissues in determining the trajectory of tissues undergoing compression in routine mammography. The skin provides a significant boundary constraint to the deformation of the interior tissues where there is a large difference in elastic values.

3) *Breast*: Voxel data from a breast were obtained from the previously described breast CT scanner [1]. After segmentation into glandular, fat, and skin tissues as previously described and shown in Fig. 7, Young's moduli were set to 88.0 kPa for skin, 10.0 kPa for gland, and 1.0 kPa for fat, with a Poisson's ratio of 0.490 (Table I). Next a series of progressively greater initial

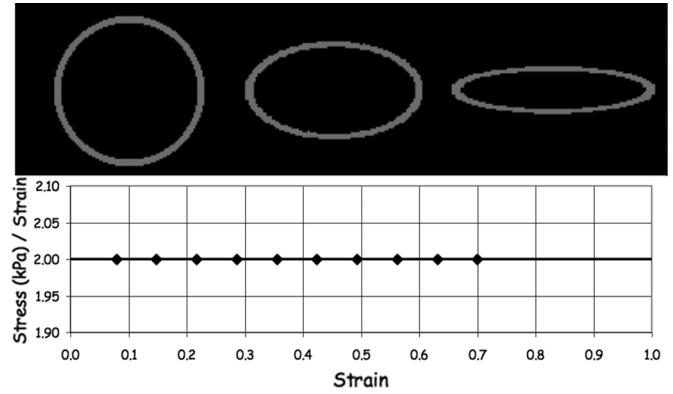


Fig. 5. Comparison of simulation with theory for a spherical shell. The shell and the surrounding material had a Young's modulus of 2.0 kPa and a Poisson's ratio of 0.490. (a) Upper panel: a subset of the 10 steps showing the response to variations in the initial applied strain  $\varepsilon_{\text{macro}}$  at values of 0.0, 0.35 and 0.70. (b) Lower panel: comparison of simulation (symbol) with theory (line). There is excellent agreement between theory and simulation ( $\rho$  = 1.00).

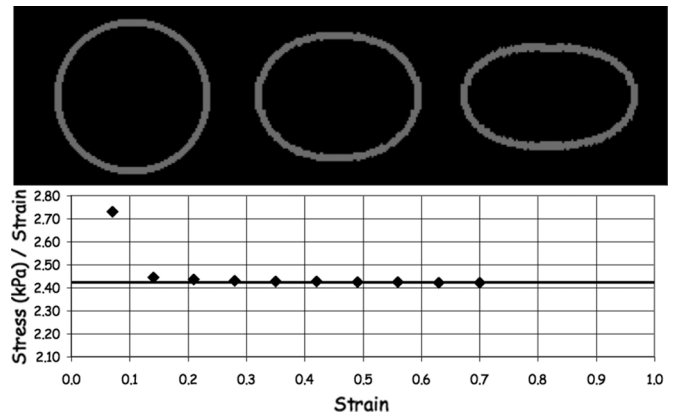


Fig. 6. Compression of a spherical shell. Young's modulus of shell is 90.0 kPa; Young's moduli of interior region and exterior region is 2.0 kPa. (a) Upper panel: a subset of the 10 steps showing the response to variations in the initial applied strain  $\varepsilon_{\text{macro}}$  at values of 0.0, 0.35 and 0.70. (b) Lower panel: change in elastic constant with compression.

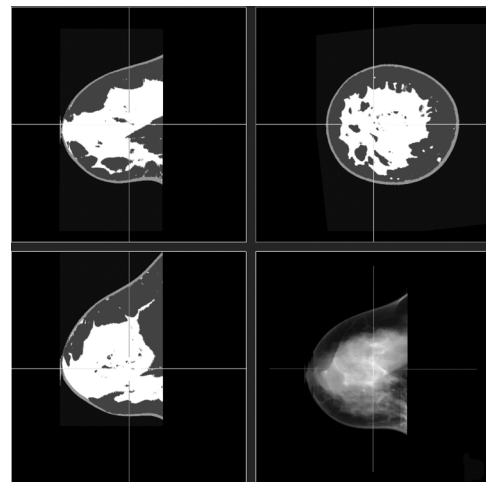


Fig. 7. Segmented  $512^3$  volume displayed showing coronal, axial, and sagittal views plus a craniol-caudal projection view for a breast composed of: skin (9%), gland (34%) and fat (57%).

compressive strains from 0.0 to 0.7 were applied with a convergence criteria of  $10^{-7}$ . The results are shown Fig. 8.

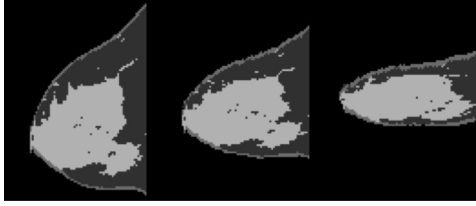


Fig. 8. Compression of segmented breast shown in Fig. 7 downsampled to  $128^3$  for the compression algorithm. The breast is composed of: skin (9%), gland (34%) and fat (57%). Young's modulus of skin is 88.0 kPa; of gland is 10.0 kPa and of fat is 1.0 kPa. The response to variations in the initial applied strain  $\epsilon_{\text{macro}}$  values of 0.0, 0.35 and 0.70 is shown for a subset of the 10 compression steps evaluated.

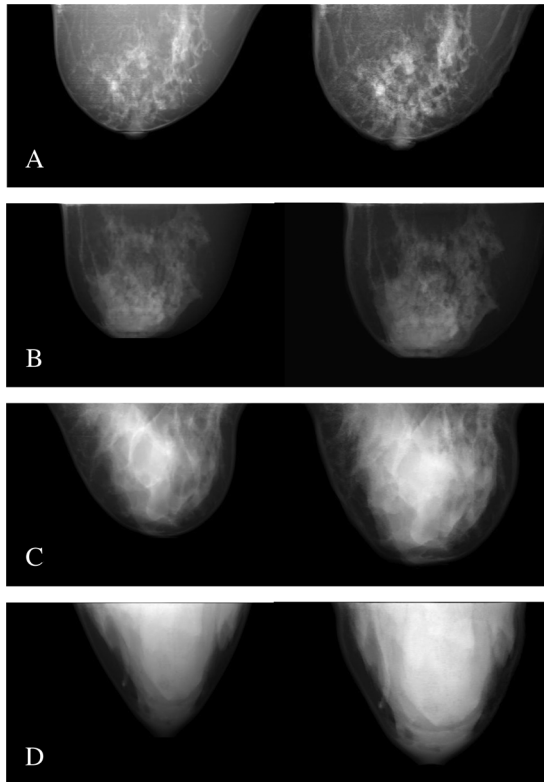


Fig. 9. Simulation of a cranio-caudal view projection mammograms (at a resolution of  $512^2$  pixels) for four different breasts of differing glandular composition [(a) 4.0% gland, (b) 12.5% gland, (c) 36.3% gland, (d) 59.5% gland] projected along the  $z$ -axis. The left images represent a projection through the uncompressed volume. The right images represent a projection through a simulation of mechanical compression, with an applied compressive strain  $\epsilon_{\text{macro}} = 0.70$ .

To demonstrate the application of the compression algorithm, we present projection mammograms for four different breast compositions, representing the range observed over our sample population [7], using simulated mechanical compression in Fig. 9. These images are obtained by integrating the intensity distribution along the  $z$ -axis, corresponding to a cranio-caudal projection. The left images represent a projection through the uncompressed volume; The right images represent a projection through a volume compressed using a simulation of mechanical compression, with an applied compressive strain  $\epsilon_{\text{macro}} = 0.70$ . The compressed images show the increase in the projection area resulting from a redistribution of tissue as the breast is compressed.

## V. DISCUSSION

Volume imaging of complex anatomic structures represents the rapidly approaching future of medical imaging. The improved clarity of structure visualization arising from volume imaging coupled with significant advantages in interactive visualization and parameter adjustment will ensure an important role in diagnosis and patient management. Projection imaging has been the historical imaging modality and despite its limitations continues to provide important diagnostic information.

Projection imaging in mammography represents the current "gold standard." Thus, technological improvements, such as from breast CT scanners or other volume imaging technologies, will need a means of comparison between modalities as part of their validation. Direct comparison is relatively straightforward between many volume and projection methods where there is essentially the same morphology present in both methods, such as with projection and CT imaging of the chest.

Breast imaging poses additional challenges since projection mammography employs significant mechanical compression of the breast to stabilize the tissues, reduce radiographic scatter, equalize the imaging pathway, and improve radiographic contrast. Breast CT imaging on the other hand does not require compression. As a consequence, comparison of breast CT and mammographic modalities requires not only transformation from volume data to projection data but also transformation from uncompressed data to mechanically compressed data. Since it is more efficient to map from  $\mathbb{R}^3$  to  $\mathbb{R}^2$  than the other way around, it becomes necessary to compress the volume data using some type of numerical compression.

The present work addresses the problem of simulating compression of volume data from breast CT. Among the various methods we considered was the use of the finite-element (FE) method. One challenge with FE methods is the task of defining an appropriate mesh with sufficient resolution to preserve structural detail without significant computational time requirements. Given the variability in breast architecture between patients, we wished to avoid the necessity of developing specialized meshes for each patient. We adapted an approach initially developed for microstructural analysis of concrete aggregates imaged using a micro-CT device employing a rectilinear grid mesh wherein each voxel in the volume represents a node in the FE mesh [2]–[4]. This approach permits assigning individual physical mechanical properties to each node based on the local tissue configuration making it an ideally matched system for compression simulation.

In this work, aimed at validating a finite-element compression algorithm using a regular rectilinear mesh, our goal was to evaluate simple objects for which independent verification was available. Following successful confirmation of algorithm performance we evaluated more complex geometries, in the form of spherical objects with various mechanical properties. Finally, we extended our analysis to segmented breast tissues obtained from a dedicated breast CT scanner.

Our overall results demonstrate that it is possible to simulate mechanical compression of a variety of objects using a regular rectilinear finite-element mesh with each node representing

specific mechanical properties. Our results also show that we can perform compression over a range of compressive strains with excellent agreement to theory. Ultimately, incorporation of multiphase tissue models with elastic properties measured from actual tissue samples will be essential to accurately determine mechanical deformation. Initial simulations using volumetric breast data from volunteers and patients and using a three-phase tissue model produced results that qualitatively are comparable to compression mammographic images. Subsequent work will evaluate a larger group of patients.

Finally, finite-element models represent a useful vehicle for simulation of mechanical compression of a range of biological tissues. Use of a rectilinear mesh that matches the coordinate system of a CT scanner significantly simplifies the challenges of mesh generation and permits direct analysis of volumetric breast data. Furthermore, the method presented here provides a robust and stable analysis. Initial results with this method show good promise in developing better mechanical compression simulations for breast CT imaging and their use in comparison to projection mammography.

#### REFERENCES

- [1] J. M. Boone, N. Shah, and T. R. Nelson, "A comprehensive analysis of DgNet coefficients for pendant-geometry cone-beam breast computed tomography," *Med. Phys.*, vol. 31, pp. 226–235, Feb. 2004.
- [2] E. J. Garboczi and A. R. Day, "An algorithm for computing the effective linear elastic properties of heterogeneous materials: Three-dimensional results for composites with equal phase Poisson ratios," *J. Mech. Phys. Solids*, vol. 43, no. 9, pp. 1349–1362, 1995.
- [3] E. J. Garboczi, Finite element and finite difference programs for computing the linear elastic and elastic properties of digital images of random materials Nat. Inst. Standards Technol., Gaithersburg, MD, Dec. 1998.
- [4] C. H. Arns, M. A. Knackstedt, W. V. Pinczewski, and E. J. Garboczi, "Computation of linear elastic properties from microtomographic images: Methodology and match to theory and experiment," *Geophysics*, vol. 67, no. 5, pp. 1396–1405, 2002.
- [5] J. M. Boone, T. R. Nelson, K. K. Lindfors, and J. A. Seibert, "Dedicated breast CT: Radiation dose and image quality evaluation," *Radiology*, vol. 221, no. 3, pp. 657–667, 2001.
- [6] C. Tanner, A. Degenhard, J. A. Schnabel, A. C. Smith, C. Hayes, L. I. Sonoda, M. O. Leach, D. Hose, D. L. G. Hill, and D. J. Hawkes, "A method for the comparison of biomechanical breast models," in *Proc. IEEE Workshop Math. Methods Biomed. Image*, Dec. 2001, pp. 11–18.
- [7] T. R. Nelson, J. Boone, J. Seibert, K. Lindfors, B. Kuhn, A. Kwan, and K. Yang, "Visualization and identification of breast glandular tissue in breast CT volume data," *Med. Phys.*, vol. 32, no. 6, p. 1897, 2005.
- [8] N. V. Ruiter, "Registration of X-ray mammograms and MR-volumes of the female breast based on simulated mammographic deformation," Ph.D. dissertation, Universität Mannheim, Mannheim, Germany, 2003.
- [9] P. R. Bakic, M. Albert, D. Brzakovic, and A. D. A. Maidment, "Mammogram synthesis using a 3D simulation. I. Breast tissue model and image acquisition simulation," *Med. Phys.*, vol. 29, no. 9, pp. 2131–2139, 2002.
- [10] J. A. Schnabel, C. Tanner, A. D. Castellano-Smith, A. Degenhard, M. O. Leach, D. R. Hose, D. L. G. Hill, and D. J. Hawkes, "Validation of nonrigid image registration using finite-element methods: Application to breast MR images," *IEEE Trans. Med. Imag.*, vol. 22, no. 2, pp. 238–247, Feb. 2003.
- [11] Y.-C. Fung, *Biomechanics: Mechanical Properties of Living Tissues*. New York: Springer-Verlag, 1981.
- [12] A. Sarvazyan, D. Goukassian, E. Maevsky, and G. Oranskaja, "Elastic imaging as a new modality of medical imaging for cancer detection," in *Proc. Int. Workshop Interaction of Ultrasound With Biological Media*, 1994, pp. 69–81.
- [13] J. B. Park, *Biomaterials Science and Engineering*. New York: Plenum, 1984.
- [14] D. L. James and D. K. Pai, "Accurate real time deformable objects," in *Proc. SIGGRAPH'99: 26th Int. Conf. Comput. Graph. Interactive Tech.*, New York, Aug. 8–13, 1999, pp. 65–72.
- [15] G. Hirota, R. Maheshwari, and M. C. Lin, "Fast volume-preserving free form deformation using multi-level optimization," in *Proc. 5th ACM Symp. Solid Modeling and Applications*, 1999, pp. 234–245.
- [16] T. Watanabe, J. Ohya, J. Kurumisawa, and Y. Tokunaga, "Real-time method for animating elastic objects' behaviors including collisions," presented at the ICAT 2003, Tokyo, Japan, Dec. 2003.
- [17] Y. C. Fung, *First Course in Continuum Mechanics (3rd Edition)*, 3rd ed. Englewood Cliffs, NJ: Prentice Hall, 1993.
- [18] W. H. Press, B. P. Flannery, S. A. Teukolsky, and W. T. Vetterling, *Numerical Recipes: The Art of Scientific Computing*. New York: Cambridge Univ. Press, 1986.



**Albert L. Kellner** received the B.S. degree in applied physics from the California Institute of Technology, Pasadena, in 1979, the M.S. degree in electrical engineering from the University of Maryland, College Park, and the Ph.D. degree in electrical engineering from the University of California at San Diego in 1991.

He is an Associate Research Scientist in the Department of Electrical and Computer Engineering at the University of California at San Diego. His research interests include biomedical imaging and

image processing.



**Thomas R. Nelson** (M'77) received the B.A. degree in mathematics and the M.S. degree in radiological physics from San Diego State University, San Diego, CA, in 1972 and 1974, respectively, and the Ph.D. degree in medical physics from the University of California at Los Angeles in 1977.

He is a Professor in the Department of Radiology at the University of California at San Diego. His research interests include medical imaging including breast imaging and 3-D ultrasound, computer modeling, and visualization.



**Laura I. Cerviño** received the B.S. degree in aeronautical engineering from Escuela Politécnica de Madrid, Spain, in 1999, and the M.S. and Ph.D. degrees in aerospace engineering from the University of California at San Diego in 2001 and 2005, respectively.

She is a Post-Doctoral Fellow at the University of California at San Diego. Her research interests include biomechanics, fluid dynamics, and system control and optimization.



**John M. Boone** (M'84) received the B.A. degree in biophysics from the University of California at Berkeley in 1979, and the M.S. and Ph.D. degrees in radiological science from the University of California at Irvine in 1981 and 1985, respectively.

He is a Professor of Radiology and Biomedical Engineering at the University of California at Davis. His research interests include the development and analysis of X-ray detector systems for earlier breast cancer detection.